Gyrotactic suppression and emergence of chaotic trajectories of swimming particles in three-dimensional flows

S. I. Heath Richardson,[1] A. W. Baggaley,[2,3] and N. A. Hill[1]

[1]*School of Mathematics and Statistics, University of Glasgow, Glasgow G12 8SQ, United Kingdom*

[2]*School of Mathematics and Statistics, Newcastle University, Newcastle upon Tyne NE1 7RU, United Kingdom*

[3]*Joint Quantum Centre Durham-Newcastle, Newcastle upon Tyne NE1 7RU, United Kingdom*

(Received 20 May 2016; published 23 February 2018)

We study the effects of imposed three-dimensional flows on the trajectories and mixing of gyrotactic swimming microorganisms and identify phenomena not seen in flows restricted to two dimensions. Through numerical simulation of Taylor-Green and Arnold-Beltrami-Childress (ABC) flows, we explore the role that the flow and the cell shape play in determining the long-term configuration of the cells' trajectories, which often take the form of multiple sinuous and helical "plumelike" structures, even in the chaotic ABC flow. This gyrotactic suppression of Lagrangian chaos persists even in the presence of random noise. Analytical solutions for a number of cases reveal the how plumes form and the nature of the competition between torques acting on individual cells. Furthermore, studies of Lyapunov exponents reveal that, as the ratio of cell swimming speed relative to the flow speed increases from zero, the initial chaotic trajectories are first suppressed and then give way to a second unexpected window of chaotic trajectories at speeds greater than unity, before suppression of chaos at high relative swimming speeds.

DOI: 10.1103/PhysRevFluids.3.023102

I. INTRODUCTION

The behavior of swimming microorganisms in active suspensions [1,2] is crucial in the survival of species, since it allows them to attain favorable locations in relation to resources, predators, and each other. Modeling the spatiotemporal population dynamics has a rich history due to the importance of unicellular organisms such as phytoplankton in ocean currents [3]. Phytoplankton are responsible for the production of half of the world's oxygen from biomass and form the base of the aquatic food chain. Identifying optimal distributions may also have applications [4,5] in biofuel production [6], which is becoming increasingly important for our planet's long-term sustainability. Orientation due to bottom heaviness (gyrotaxis), or equivalently negative buoyancy plus body shape (rheotaxis), is a feature of many free-swimming microorganisms such as the ubiquitous freshwater single-cell green alga *Chlamydomonas reinhardtii* and the single-cell, green-alga genus *Dunaliella* found in salt water.

Being bottom heavy, gyrotactic cells experience a gravitational torque which acts to reorient them if they move away from their preferred vertical orientation. Consequently cells focus into downwelling regions resulting in the formation of plumes. Irrespective of shape, orientation will also be affected by local vorticity in the fluid, while nonspherical cells may experience an additional torque due to the rate of strain. The balance of these torques and their effect on trajectories is examined in this paper.

Torney and Neufeld [7] and Khurana *et al.* [8,9] computed the dynamics of freely rotating prolate swimming particles in both steady and unsteady two-dimensional (2D) imposed laminar test flows consisting of periodic sinusoidal vortices given by a stream function of the form

$$\psi(x,y,t) = U[\sin(x + B\sin(\Omega t))]\sin y, \tag{1}$$

where x and y are Cartesian coordinates, t is time, U is the maximum flow speed, Ω is the angular frequency of the lateral oscillation of the flow, and B is its amplitude. For steady flows ($B = 0$), cell trajectories divide into two regions at slow swimming speeds. In one region, cells aggregate around the boundaries of the vortices with chaotic trajectories that move between vortices. In the other region, cells are trapped within chaotic domains in centers of the vortices, but above a threshold speed the particles escape from this regular elliptic region. For thin rodlike particles, the threshold velocity decreases to zero so that there are no barriers to transport across cells. Furthermore, as the swimming velocity increases, the rate of particle transport can decrease due to the formation of traps near elliptic islands that hold swimming cells for long times. This effect is enhanced for more elongated particles and when stochastic terms are added to the swimming model. At higher swimming speeds, rodlike cells are attracted to stable manifolds of hyperbolic fixed points.

In a recent numerical study, Durham *et al.* [10] examined the behavior of gyrotactic, spherical cells in a 2D imposed flow and discovered both regimes in which the cells were concentrated into patterns and in which they were randomly distributed.

When, in addition to a 2D flow, the orientation of gyrotactic swimming cells is restricted to two dimensions as in [10], cells tumble when vorticity is high, but with realistic *unrestricted three-dimensional (3D) orientation* (even in a 2D flow), cells reorient in the third (crossflow) dimension and spin about their axis, so that the cell swimming direction has an additional degree of freedom, as shown by Pedley and Kessler (Sec. 3.1 of [11]). This means that even the components of the mean cell swimming speed projected onto the 2D plane are different when the cells are allowed unrestricted 3D orientation.

Thorn and Bearon [5] investigated the transport and dispersion of spherical gyrotactic organisms with 3D orientation in steady 2D homogeneous linear shear flows, with and without additive stochastic reorientation. Gyrotaxis in fully developed turbulent flows was also studied by them and more recently in [12,13].

However, there are few studies in steady inhomogeneous three-dimensional flows which increase the complexity by introducing mixing and Lagrangian chaos [14,15], but remain amenable to analytical progress. In this paper, we fill this gap in knowledge and relax the unphysical restrictions in [10] by allowing the cells to orient in three dimensions and investigating the role of cell shape in inhomogeneous three-dimensional test flows for ellipsoidal cells subject to gyrotaxis. We identify phenomena not seen in flows restricted to two dimensions.

II. MODEL FORMULATION

We consider two incompressible velocity fields. The first is the Taylor-Green vortex (TGV) flow, where the fluid velocity is [16,17]

$$\boldsymbol{u} = \begin{pmatrix} -2\cos x \sin y \sin z \\ \sin x \cos y \sin z \\ \sin x \sin y \cos z \end{pmatrix}. \tag{2}$$

Here $\boldsymbol{x} = (x, y, z)^T$ is the laboratory-frame position vector in Cartesian coordinates where x and y are the horizontal components and z is vertically upwards. This is a very commonly used test flow, both due to its tractability and because it represents an exact closed-form solution of the incompressible Euler equations. The streamlines are steady closed counter-rotating vortices, and the vorticity is

$$\boldsymbol{\omega} \equiv \nabla \times \boldsymbol{u} = 3\cos x \begin{pmatrix} 0 \\ -\sin y \cos z \\ \cos y \sin z \end{pmatrix}. \tag{3}$$

[Note that Eq. (1) is a 2D TGV flow when $B = 0$.]

Second, we impose the Arnold-Beltrami-Childress (ABC) flow [18]:

$$\boldsymbol{u} = \begin{pmatrix} \cos y + \sin z \\ \cos z + \sin x \\ \cos x + \sin y \end{pmatrix}. \tag{4}$$

This is a more complex but consequently biologically relevant flow as it exhibits Lagrangian chaos. It also possesses the Beltrami property that $\boldsymbol{u} = \boldsymbol{\omega}$ and has open streamlines [19].

Each velocity field requires a separate nondimensionalization. The same scaling as in [10] has been used in Eq. (1) for the TGV flow; i.e., lengths have been scaled by $L/2\pi$, velocities by $L\omega_0/2\pi$, vorticity by ω_0, and time by $1/\omega_0$, where L is the spacing between the cube of adjacent vortices in the flow and ω_0 is the maximum vorticity at the center of these vortices. For the ABC flow in Eq. (2), lengths are nondimensionalized by $1/2\pi$, velocities by u_0, vorticity by $2\pi u_0$, and time by $1/2\pi u_0$, where u_0 is the maximum fluid velocity.

The swimming cells are modeled as gyrotactic prolate ellipsoids and are so small ($\approx 10-20\,\mu$m) that the local Reynolds number is effectively zero. Using the well-established model of Pedley and Kessler [20], the nondimensionalized equations determining cell orientation $\boldsymbol{p}$ and position $\boldsymbol{x}$ are the gyrotaxis equation,

$$\dot{\boldsymbol{p}} \equiv \frac{d\boldsymbol{p}}{dt} = \frac{1}{2G}[\boldsymbol{k} - (\boldsymbol{k}\cdot\boldsymbol{p})\boldsymbol{p}] + \frac{1}{2}(\boldsymbol{\omega}(\boldsymbol{x}) \times \boldsymbol{p}) + \alpha \boldsymbol{f}, \tag{5}$$

and the cell velocity equation,

$$\dot{\boldsymbol{x}} \equiv \frac{d\boldsymbol{x}}{dt} = V\boldsymbol{p} + \boldsymbol{u}(\boldsymbol{x}). \tag{6}$$

Here $\boldsymbol{f} = (\boldsymbol{I} - \boldsymbol{pp})\cdot\boldsymbol{E}(\boldsymbol{x})\cdot\boldsymbol{p}$ and $\boldsymbol{E}(\boldsymbol{x})$ is the rate-of-strain tensor, which has components

$$E_{ij} = (\partial u_i/\partial x_j + \partial u_j/\partial x_i)/2 \qquad \forall\, i,j = 1,2,3. \tag{7}$$

In Eqs. (5) and (6), the unit vector $\boldsymbol{k}$ defines the preferred swimming direction of cells which is vertically upwards, $\boldsymbol{I}$ is the identity tensor, t is time, V defines the swimming speed of cells relative to the flow, and G describes the rate of gyrotactic reorientation. When $G \ll 1$ cells tend to swim vertically upwards regardless of the ambient flow, and as $G \to \infty$ the cells rotate freely in the flow. The cell eccentricity is $\alpha = (a^2 - b^2)/(a^2 + b^2)$, where a and b are the lengths of a cell's semimajor axis and minor axis, respectively. Note that $\alpha = 0$ describes a sphere (e.g., a spherical squirmer [21]) and $\alpha = 1$ a thin rod. Here we assume that the suspension is sufficiently dilute that cell-cell interactions can be neglected and the cells have no influence on the bulk flow. Equations (5) and (6) are expanded below for later reference:

$$\dot{\boldsymbol{p}} = \begin{pmatrix} -\frac{p_x p_z}{2G} + \frac{\omega_y p_z - \omega_z p_y}{2} + \alpha f_x \\ -\frac{p_y p_z}{2G} + \frac{\omega_z p_x - \omega_x p_z}{2} + \alpha f_y \\ \frac{1-p_z^2}{2G} + \frac{\omega_x p_y - \omega_y p_x}{2} + \alpha f_z \end{pmatrix} \tag{8}$$

and

$$\dot{\boldsymbol{x}} = \begin{pmatrix} V p_x + u_x \\ V p_y + u_y \\ V p_z + u_z \end{pmatrix}, \tag{9}$$

where

$$\begin{aligned} f_x = {} & E_{11}p_x\left(1 - p_x^2\right) + E_{12}p_y\left(1 - 2p_x^2\right) + E_{13}p_z\left(1 - 2p_x^2\right) \\ & - E_{22}p_y^2 p_x - 2E_{23}p_x p_y p_z - E_{33}p_x p_z^2, \end{aligned} \tag{10}$$

$$f_y = -E_{11}p_x^2 p_y + E_{12}p_x\left(1-2p_y^2\right) - 2E_{13}p_x p_y p_z + E_{22}p_y\left(1-p_y^2\right) + E_{23}p_z\left(1-2p_y^2\right) - E_{33}p_y p_z^2, \tag{11}$$

$$f_z = -E_{11}p_x^2 p_z - 2E_{12}p_x p_y p_z + E_{13}p_x\left(1-2p_z^2\right) - E_{22}p_y^2 p_z + E_{23}p_y\left(1-2p_z^2\right) + E_{33}p_z\left(1-p_z^2\right). \tag{12}$$

Cartesian coordinates are retained in Eq. (8) instead of converting to spherical polars [11] to avoid potential computational difficulties at the poles.

For direct numerical simulation of the cells' trajectories in the TGV and ABC flows, a fourth order Runge-Kutta scheme with a time step of $\delta t = 0.01$ was implemented; simulations with $\delta t = 0.005$ were also carried out as a convergence check. Each simulation was initialized with 1000 cells with random orientations and positions in a $(2\pi)^3$ box with periodic boundary conditions on all sides.

For both of the three-dimensional TGV and ABC flows, we explore the parameter ranges

$$(G,V) \in (0,10) \times (0,10) \quad \text{and} \quad 0 \leqslant \alpha \leqslant 1.0.$$

No qualitatively new features were found outside this range, and moreover we note that in their example of 2D flow with 2D trajectories, Durham *et al.* [10] did cover a wider parameter range $(G,V) \in (10^{-2},10^2) \times (10^{-2},10^2)$ but the extreme ranges show no additional patterns.

III. TAYLOR-GREEN VORTEX FLOW

For all values of G and α, simulating passive tracers with $V = 0$ results in no discernible pattern, with cells instead remaining randomly spread as $t \to \infty$, with each cell remaining within its initial vortex. When $V > 0$, cells can swim across streamlines and are no longer confined to a single vortex. Setting $G = 1$ for a slow swimming speed $V = 0.025$ results in slight clustering around $y = \pi/2$ and $3\pi/2$. Increasing the swimming speed to $V = 0.1$ results in the cells forming the organized structures shown in Fig. 1. When $\alpha = 0, 1/2$, the system collapses onto two sheets at $y = \pi/2$ and $3\pi/2$ so that cell movement is exclusively in the xz plane. For both of these eccentricities cells form structures that almost exclusively follow the streamlines of the flow due to their relatively low swimming speed. When $V \approx 0.15$ any structure degenerates and as $t \to \infty$ cell trajectories again appear to be random. In general, organized structures do not always develop but are instead only found for specific parameter ranges.

Simulating spherical cells with $V = 1$ and $G = 0.1$ results in all trajectories tending to one of four distinct points,

$$\left(\frac{3\pi}{2},\frac{3\pi}{2},\pi\right), \left(\frac{\pi}{2},\frac{\pi}{2},\pi\right), \left(\frac{\pi}{2},\frac{3\pi}{2},0\right), \left(\frac{3\pi}{2},\frac{\pi}{2},0\right),$$

where cells subsequently settle and orient upwards, i.e., $\boldsymbol{p} = (0,0,1)^T$. Cells are now positioned so that up-swimming exactly cancels the fluid velocity and a fixed steady state has been reached. Substituting these values of $\boldsymbol{x}$ and $\boldsymbol{p}$ into Eqs. (5) and (6) confirms that $\dot{\boldsymbol{p}} = \dot{\boldsymbol{x}} = \boldsymbol{0}$. These single-point solutions are also seen in Table II when $\alpha = 0$, $V = 1$, and $G = 1$, just above "∞-shaped" closed-loop trajectories reminiscent of Bowditch-Lissajous figures [22] that lie in the planes $y = \pi/2$ and $y = 3\pi/2$.

Examination of intermediate speeds reveals a number of diverse formations, three of which are seen in Fig. 2. Projections of these patterns are shown in Figs. 3(a)–3(c). Simulating with the parameters $\alpha = 0$, $V = 3$, and $G = 1$ produces four curved plumes in the yz plane. From Fig. 3(a), we observe that $p_x = 0$ and the trajectories lie in the planes $x = \pi/2$ and $x = 3\pi/2$, on which the vorticity

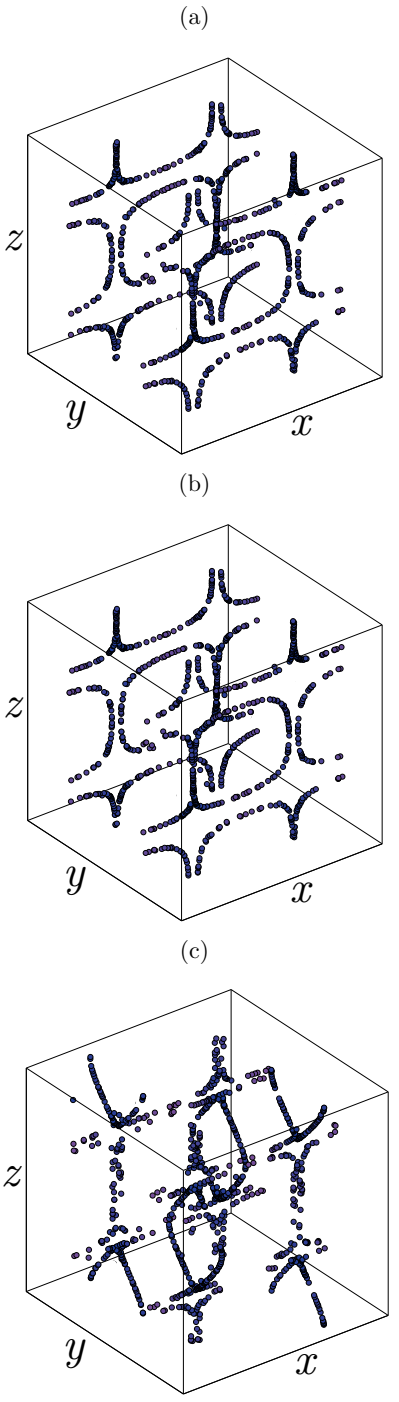

FIG. 1. Simulations of cells in the TGV flow with $V = 0.1$ and $G = 1$: (a) $\alpha = 0$, (b) $\alpha = 0.5$, and (c) $\alpha = 1$.

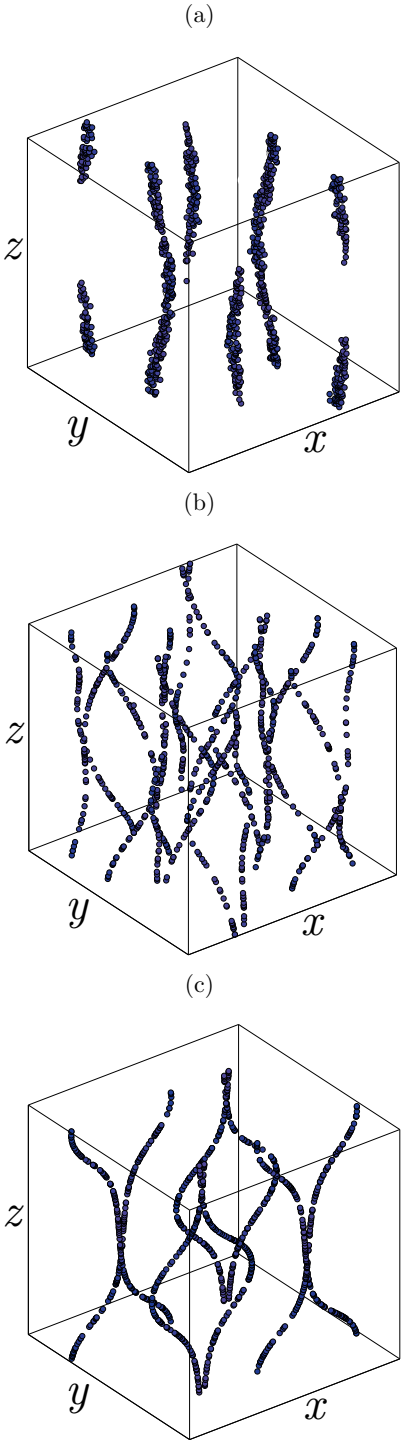

FIG. 2. Simulations of cells in the TGV flow with $V = 3$ and $G = 1$: (a) $\alpha = 0$, (b) $\alpha = 0.5$, and (c) $\alpha = 1$.

(a) $\alpha = 0$

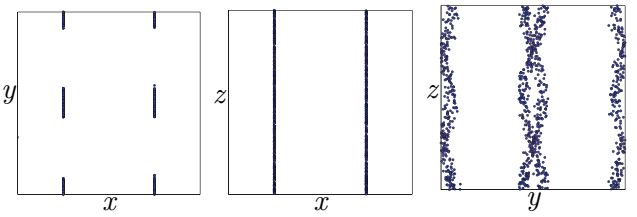

(b) $\alpha = 1$. The red and blue arrows show trajectories formed using (18) when $p_x = \pm 0.6$ respectively.

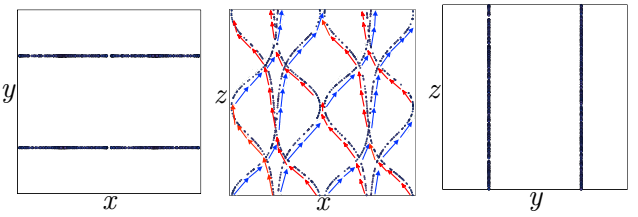

(c) $\alpha = 1/2$.

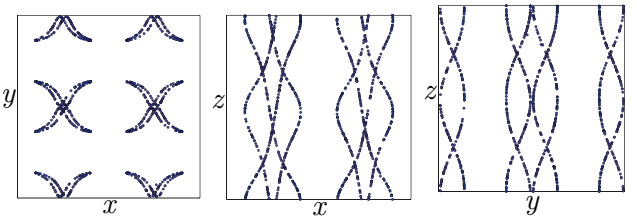

FIG. 3. Projections of cell trajectories in the TGV flow for $V = 3$ and $G = 1$.

vanishes [see Eq. (3)]. Substituting these values into Eqs. (8) and (9) yields

$$\dot{\boldsymbol{p}} = \begin{pmatrix} 0 \\ -\frac{p_y p_z}{2G} \\ \frac{1-p_z^2}{2G} \end{pmatrix} \tag{13}$$

and

$$\dot{\boldsymbol{x}} = \begin{pmatrix} 0 \\ V p_y \pm \cos y \sin z \\ V p_z \pm \sin y \cos z \end{pmatrix}. \tag{14}$$

The general solution of Eq. (13) is

$$\boldsymbol{p} = \begin{pmatrix} 0 \\ De^{-t/2G} \\ \frac{Ce^{t/G}-1}{1+Ce^{t/G}} \end{pmatrix}, \tag{15}$$

where C and D are arbitrary constants. Taking the limit as $t \to \infty$ and inserting into Eq. (14) yields

$$\dot{\boldsymbol{x}} = \begin{pmatrix} 0 \\ \pm \cos y \sin z \\ V \pm \sin y \cos z \end{pmatrix}. \tag{16}$$

These equations now define a simple two-dimensional flow with closed streamlines, and plotting particle trajectories reveals a similar pattern to that in Fig. 3(a).

For rodlike cells ($\alpha = 1$), clustering again occurs leading to the formation of four plumes, now in the xz plane. From Fig. 3(b), it is clear that

$$p_y = 0 \quad \text{and} \quad y = \pi/2 \quad \text{or} \quad 3\pi/2,$$

which are inserted into Eqs. (5) and (6) to obtain

$$\dot{\boldsymbol{p}} = \begin{pmatrix} -\frac{p_x p_z}{2} \pm g_x \\ 0 \\ \frac{1-p_z^2}{2} \pm g_z \end{pmatrix} \tag{17}$$

and

$$\dot{\boldsymbol{x}} = \begin{pmatrix} 3p_x \pm 2\cos x \sin z \\ 0 \\ 3p_z \pm \sin x \cos z \end{pmatrix}, \tag{18}$$

where

$$g_x = p_z\left(-2 + p_x^2\right)\cos x \cos z + p_x\left(2 - 2p_x^2 + p_z^2\right)\sin x \sin z, \tag{19}$$

$$g_z = (p_x/2)\left(5/2 + p_z^2\right)\cos x \cos z + p_z\left(-2p_x^2 - 1 + p_z^2\right)\sin x \sin z. \tag{20}$$

As $\alpha > 0$, cells are now be affected by the rate of strain in the flow, so that the complexity of Eq. (17) is increased and an analytical solution cannot be obtained. However, tracking the orientation of cells numerically for large values of t shows that

$$-0.6 < p_x < 0.6, \quad p_y = 0, \quad \text{and} \quad 0.8 < p_z < 1,$$

which is consistent with the xz view in Fig. 3(b). Particle trajectories can again be plotted using Eq. (18). Without an analytical solution for Eq. (17) we must now select a few of the extreme values of p_x and p_z to gain a structure comparable to Fig. 3(b). This can be seen in the xz view of Fig. 3(b), in which red arrows show the trajectories when $p_x = -0.6$ and the blue dashed arrows correspond to $p_x = 0.6$.

Lastly, trajectories for which $\alpha = 1/2$ are examined. Figure 3(c) shows that cells now form an intricate structure involving eight curved plumes on one-dimensional manifolds. Since $\alpha \neq 0$, an analytical solution again cannot be found for Eq. (8), but moreover as cells now continue to move in all three planes, Eq. (9) cannot be simplified. However, this does demonstrate the importance of cell shape, with α acting as a bifurcation parameter. Recalling Fig. 2, a pattern involving four plumes in the yz plane was seen for spherical cells ($\alpha = 0$), simulating rods ($\alpha = 1$) resulted in four plumes in the xz plane, while $\alpha = 1/2$ gives eight plumes on one-dimensional manifolds. Thus varying eccentricity affects both the number and location of plumes, while we conclude that increasing α leads to more complex structures, or cells follow three-dimensional flow and any clustering breaks down, leading to full mixing [23,24].

As V increases, the diversity in behavior subsides and when $V \gtrsim 5$ cells only form the upwelling structures seen in Fig. 4. Spherical cells collect in two sheets in the yz plane, while clustering results in four upwelling plumes when $\alpha = 1/2$ and $\alpha = 1$. In Fig. 4, irrespective of shape,

$$\boldsymbol{p} = (0,0,1)^T \quad \text{and} \quad x = \pi/2 \quad \text{or} \quad 3\pi/2,$$

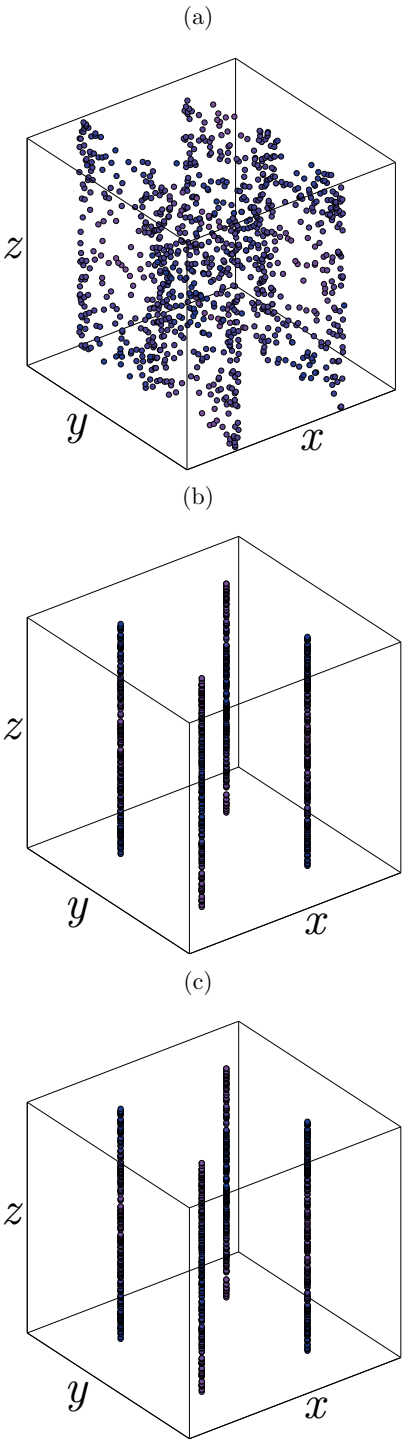

FIG. 4. Simulations of cells in the TGV flow with $V = 9$ and $G = 1$: (a) $\alpha = 0$, (b) $\alpha = 0.5$, and (c) $\alpha = 1$.

TABLE I. TGV flow for values of $V < 1$, when $G = 1$.

$\alpha = 1$	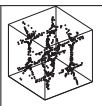	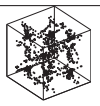	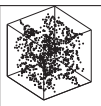	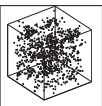	Similar to $V = 0.4$.				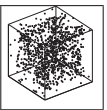
$\alpha = 0.5$	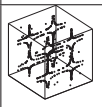	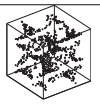	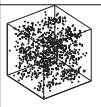	Similar to $V = 0.9$					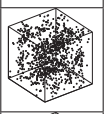
$\alpha = 0$	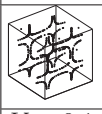	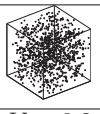	Similar to $V = 0.2$					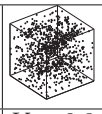	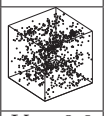
	$V = 0.1$	$V = 0.2$	$V = 0.3$	$V = 0.4$	$V = 0.5$	$V = 0.6$	$V = 0.7$	$V = 0.8$	$V = 0.9$

so Eq. (16) holds again. When $\alpha = 1/2$ and $\alpha = 1$, cells cluster at $y = \pi/2$ or $3\pi/2$, and Eq. (16) simplifies to

$$\dot{\boldsymbol{x}} = \begin{pmatrix} 0 \\ 0 \\ V \pm \cos z \end{pmatrix}.$$

Consequently, trajectories are now restricted to the vertical plumes seen in Figs. 4(b) and 4(c). This demonstrates that increasing swimming speed suppresses the effects of the surrounding flow [25]. The full range of parameter values that have been used in simulations of the TGV flow and the steady-state patterns that are found are given in Tables I and II.

IV. ABC FLOW

We now turn our attention to the more complex of the two test flows which we see does not prevent clustering despite the presence of Lagrangian chaos. Following [14], we calculate the time- and ensemble-averaged principal Lyapunov exponent for the trajectories of cells in the given flow. To be specific, the cells' initial positions are chosen randomly from a uniform distribution across the spatial domain, and their initial orientations are chosen independently from a uniform distribution on the unit sphere, the simulations are stepped forward in time until all transient effects have decayed, and then the Lyapunov exponents are evaluated for each cell, from which the mean value over all

TABLE II. TGV flow for values of $V \geqslant 1$, when $G = 1$.

$\alpha = 1$	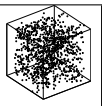		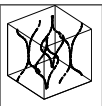	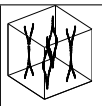	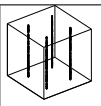	Similar to $V = 5$			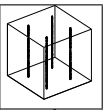
$\alpha = 0.5$	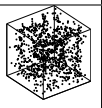	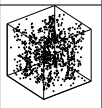	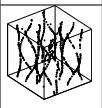		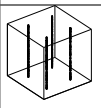	Similar to $V = 5$			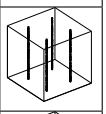
$\alpha = 0$	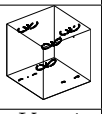	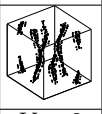	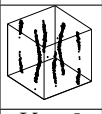	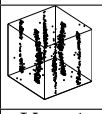	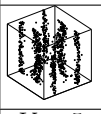	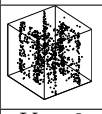	Similar to $V = 6$		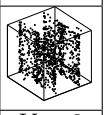
	$V = 1$	$V = 2$	$V = 3$	$V = 4$	$V = 5$	$V = 6$	$V = 7$	$V = 8$	$V = 9$

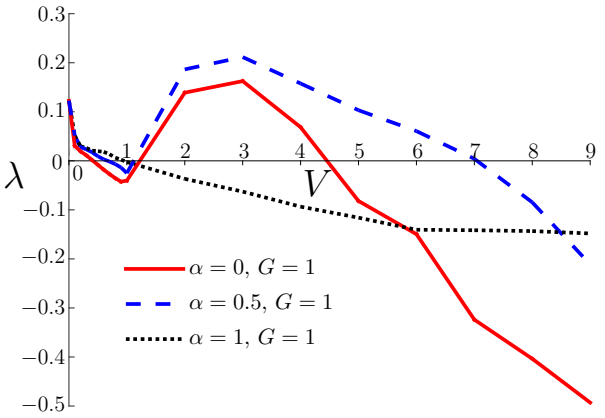

FIG. 5. Graph of the principal Lyapunov exponent when $G = 1$ corresponding to the flows illustrated in Tables III and IV, showing the existence ($\lambda > 0$) and suppression ($\lambda < 0$) of Lagrangian chaos.

cells at each time step is calculated. This mean value is then averaged over 500 time steps. Positive values of the Lyapunov exponent indicate exponential divergence of cell trajectories and hence a chaotic flow since the domain is bounded; negative values correspond to suppression of Lagrangian chaos.

Setting $V = 0$ corresponds to the cells behaving as passive tracers and, as expected, $\lambda > 0$ because the ABC flow is chaotic, and the cells become randomly distributed throughout the computational box (see Figs. 5 and 6). We now consider what happens for increasing values of V.

For all values of α, as V increases to $V \approx 1$, λ decreases and becomes negative (Figs. 5 and 6), showing that gyrotaxis suppresses Lagrangian chaos as plume formation begins to dominate. The patterns formed by the plumes are illustrated in Tables III and IV. A helical plume forms along the central axis of the box, with a secondary plume at the periodic side boundary for small nonzero values of V when $\alpha = 1$ (see, e.g., Fig. 7), together with other secondary features.

The numerical results show that the trajectories in Fig. 7(a), when $\alpha = 0$, lie on the helix

$$x = \pi + a\cos z, \quad y = 3\pi/2 - a\sin z, \tag{21}$$

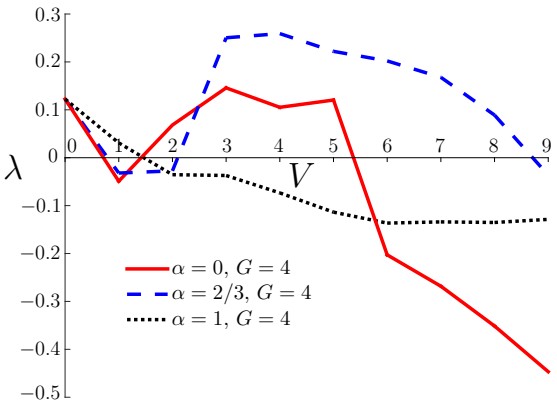

FIG. 6. Graph of the principal Lyapunov exponent when $G = 4$ corresponding to the flows illustrated in Table V, showing the existence ($\lambda > 0$) and suppression ($\lambda < 0$) of Lagrangian chaos.

TABLE III. ABC flow projected onto the $z = 0$ plane for $V < 1$, when $G = 1$.

$\alpha = 1$		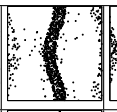	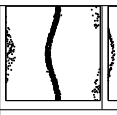	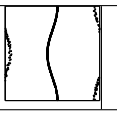	Similar to $V = 0.4$			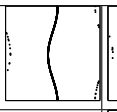	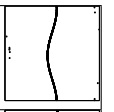
$\alpha = 0.5$		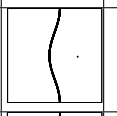	Similar to $V = 0.2$						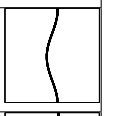
$\alpha = 0$		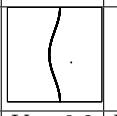	Similar to $V = 0.2$						
	$V = 0.1$	$V = 0.2$	$V = 0.3$	$V = 0.4$	$V = 0.5$	$V = 0.6$	$V = 0.7$	$V = 0.8$	$V = 0.9$

of radius $a \approx 0.35$. As a validation of the numerical results, it is possible to derive an approximate solution for this manifold as follows. Defining new coordinates $x' = x - \pi$ and $y' = y - 3\pi/2$ then, from Eq. (4), the fluid velocity and vorticity on the helix are

$$\boldsymbol{u} = \boldsymbol{\omega} = \begin{pmatrix} \sin z - \sin(a \sin z) \\ \cos z - \sin(a \cos z) \\ \cos(a \sin z) - \cos(a \cos z) \end{pmatrix} = (1 - a)\boldsymbol{e}_\theta + (-2 + a^2/2)\boldsymbol{k} + O(a^3), \tag{22}$$

using cylindrical polar coordinates (r,θ,z) with unit base vectors $\boldsymbol{e}_r$, $\boldsymbol{e}_\theta$, and $\boldsymbol{k}$. Dropping the primes, the position of a cell on the helix is

$$\boldsymbol{x} = a\boldsymbol{e}_r(\theta(t)) + z(t)\boldsymbol{k} \Rightarrow \dot{\boldsymbol{x}} = -a\sigma\boldsymbol{e}_\theta + \sigma\boldsymbol{k}, \tag{23}$$

where $z = -\theta = \sigma t$ and $\sigma < 0$ is a constant speed. From Eq. (6),

$$V\boldsymbol{p} = p_\theta\boldsymbol{e}_\theta + p_z\boldsymbol{k} + O(a^3), \quad \text{where} \tag{24}$$

$$p_\theta = [a(1 - \sigma) - 1], \quad p_z = [2 + \sigma - a^2/2] \Rightarrow V\dot{\boldsymbol{p}} = \sigma p_\theta \boldsymbol{e}_r + O(a^3). \tag{25}$$

Noting that

$$\omega \wedge V\boldsymbol{p} = \sigma(1 - 3a)\boldsymbol{e}_r + O(a^2)$$

TABLE IV. ABC flow projected onto the $z = 0$ plane for values of $V \in [1,9]$, when $G = 1$.

$\alpha = 1$	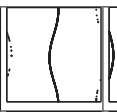	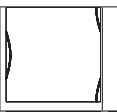	Similar to $V = 2$						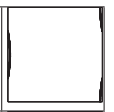
$\alpha = 0.5$		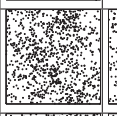	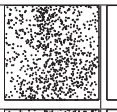		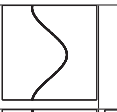	Similar to $V = 5$			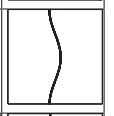
$\alpha = 0$		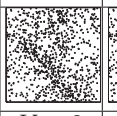	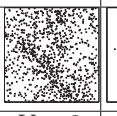	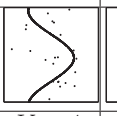	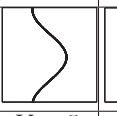	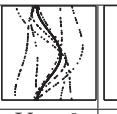	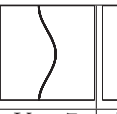	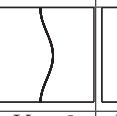	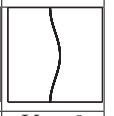
	$V = 1$	$V = 2$	$V = 3$	$V = 4$	$V = 5$	$V = 6$	$V = 7$	$V = 8$	$V = 9$

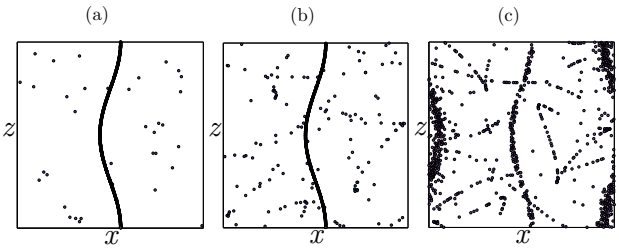

FIG. 7. Simulations of cells in the ABC flow with $V = 0.1$ and $G = 1$: (a) $\alpha = 0$, (b) $\alpha = 0.5$ and (c) $\alpha = 1$.

and

$$\boldsymbol{k} - (\boldsymbol{k}\cdot\boldsymbol{p})\boldsymbol{p} = -p_z p_r \boldsymbol{e}_r - p_\theta p_z \boldsymbol{e}_\theta + (1 - p_z^2)\boldsymbol{k},$$

equating coefficients in Eq. (5) and assuming that

$$V = \widetilde{V}a^2, \quad \text{where} \quad \widetilde{V} = O(1),$$

yields

$$a = 1/3 \quad \text{and} \quad \sigma = -2 + (1 + \widetilde{V})a^2 + O(a^3),$$

which is consistent with the numerical estimates from the simulations. The value of a ensures that $\omega \wedge \boldsymbol{p} = 0$ while the value of σ renders $p_z \approx 1$. To this order, we see that the shape of the manifold is independent of G, and $p_r = p_\theta = O(a^2)$, so that the cells are swimming vertically upwards while being carried downwards in the flow on the helical trajectory.

When V is increased further and the swimming cells move more rapidly through the flow field, λ increases and becomes positive as a second window of chaotic trajectories is encountered, provided $\alpha < 1$. Figure 8 illustrates that the window exists for a wide range of values of $G \geqslant 1$. Finally as $V \to \infty$, the cells move so quickly that plumes form once again and λ decreases through zero as chaotic trajectories are suppressed. Patterns transition from the second chaotic window through complicated braided patterns that are spatially periodic in the vertical direction with wavelengths that are multiples of 2π, the height of the computational box. Examples are described in more detail below. At very large values of V, single helical plumes are found in the same region of the box as

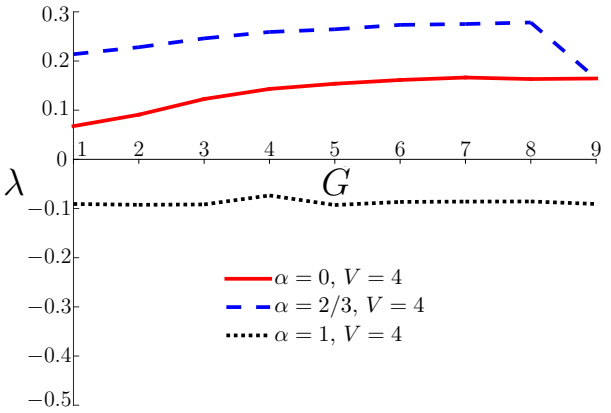

FIG. 8. Graph of the principal Lyapunov exponent when $V = 4$ corresponding to the flows illustrated in Table VI, showing the existence ($\lambda > 0$) and suppression ($\lambda < 0$) of Lagrangian chaos.

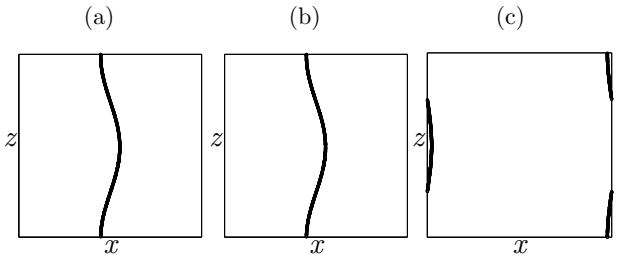

FIG. 9. Simulations of cells in the ABC flow with $V = 9$ and $G = 1$: (a) $\alpha = 0$, (b) $\alpha = 0.5$, and (c) $\alpha = 1$.

when $0 < V < 1$, but now they have the opposite sense and cells are no longer carried downwards in the local flow (see, e.g., Fig. 9). The case $\alpha = 1$ (rodlike cells) appears to be singular, in that there is no second window of chaos and plumes form in different quadrants of the computational domain. In the Discussion below, we give evidence that in this limit, orientation by gyrotaxis and by the local rate of strain in the flow exactly cancel along plume axes.

For parameter ranges which produce organized structures, cell trajectories are periodic; this is illustrated in Fig. 10, where the evolution as swimming speed increases is examined. For cells in a downwelling plume, as V increases so does the time taken to complete a circuit, due to the cells' preferred direction being upwards while the region of accumulation promotes downward movement.

Cells with low speeds tend to move with the flow resulting in short periods. However, as V increases, cells are able to more effectively counter the flow before reaching a bifurcation point at $V \approx 1.4$, where the downward motion is entirely suppressed and only an upwelling plume is formed. The region between the dashed black lines in Fig. 10 indicate swimming speeds where both down and/or upwelling plumes form in different regions of the same flow, as the parameter V is varied.

The outcome of simulations for $V = 4$ and $G = 4$ is seen in Fig. 11. Views projected onto different planes when $\alpha = 2/3$ are seen in Fig. 12. This gives one of the most intricate structures observed, and again features a plume on a one-dimensional manifold. Tracking orientation, it was observed

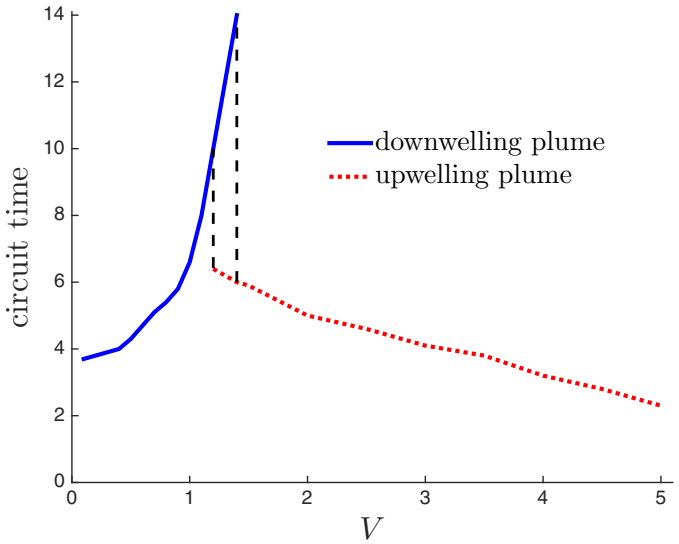

FIG. 10. Time for cells to complete one circuit of a plume when $G = 0.1$ and $\alpha = 0$.

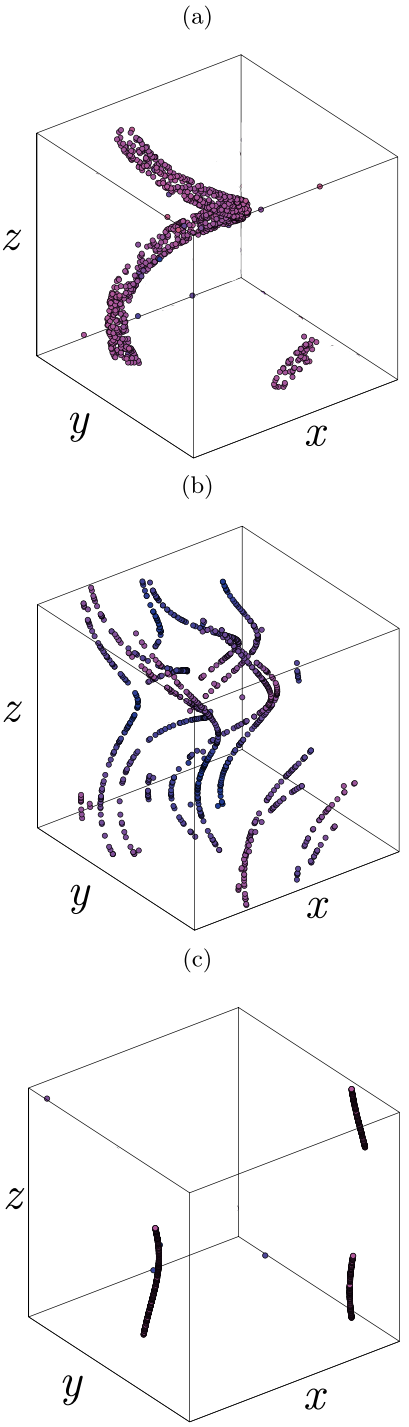

FIG. 11. Simulations of cells in the ABC flow with $V = 4$ and $G = 4$: (a) $\alpha = 0$, (b) $\alpha = 2/3$, and (c) $\alpha = 1$.

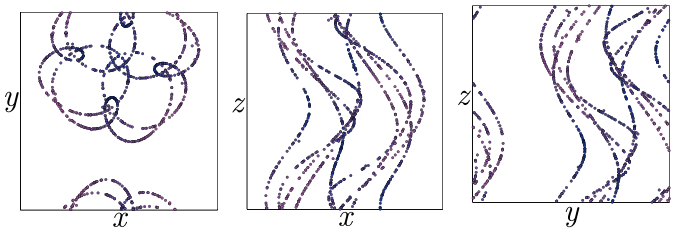

FIG. 12. Projections of cell trajectories in the ABC flow with $\alpha = 2/3$, $V = 4$, and $G = 4$.

that

$$-0.5 < p_x < 0.5, \quad -0.5 < p_y < 0.5, \quad 0.88 < p_z < 1.$$

Solutions were found to be periodic, with period equal to 19.03, during which time each cell travels along all of the nine trajectories in the periodic box. Alternatively, one may think of this as a single trajectory extending through nine vertically connected boxes. Figure 13 shows how p_x varies during this periodic circuit. Decomposition into Fourier series reveals that the dominant frequency is related to the number of times a cell crosses the box in the z direction.

To study the movement of cells relative to each other, the nearest neighbor distance was calculated after aggregation had occurred and then tracked over a long time period. The results for several different structures are seen in Fig. 14. Comparing the results for random arrangements to those which have formed plumes provides clear evidence that the formation of these structures has led to a suppression of the Lagrangian chaos.

Figure 11 also illustrates the importance of cell shape on trajectories. When $\alpha = 0$, a simple plume forms, whereas taking $\alpha = 2/3$ results in a more complex braided structure. Closer investigation revealed this braiding only occurs for $0.66 \lesssim \alpha \lesssim 0.72$, showing how small the window for this behavior to occur is. When $\alpha = 1$, a single plume at the periphery of the box is seen.

The full range of parameter values that have been used in simulations of the ABC flow and the steady-state patterns are given in Tables III–VI, and in the Supplemental Material [26].

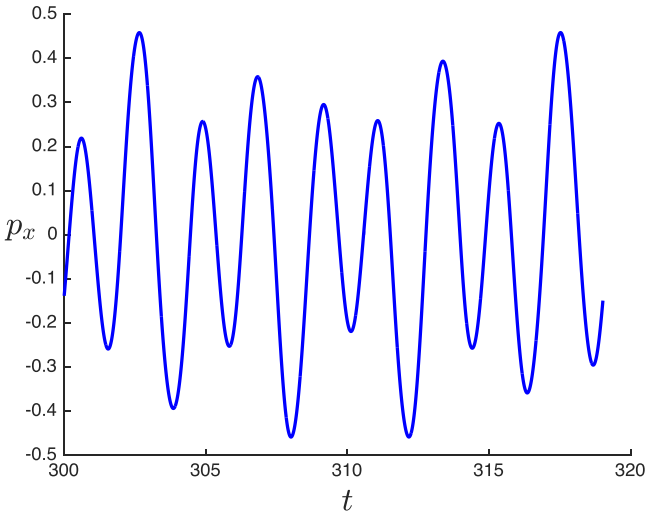

FIG. 13. Change in p_x for one period from $t = 300$ to 319.03 for the ABC flow with $V = 4$, $G = 4$, and $\alpha = 2/3$.

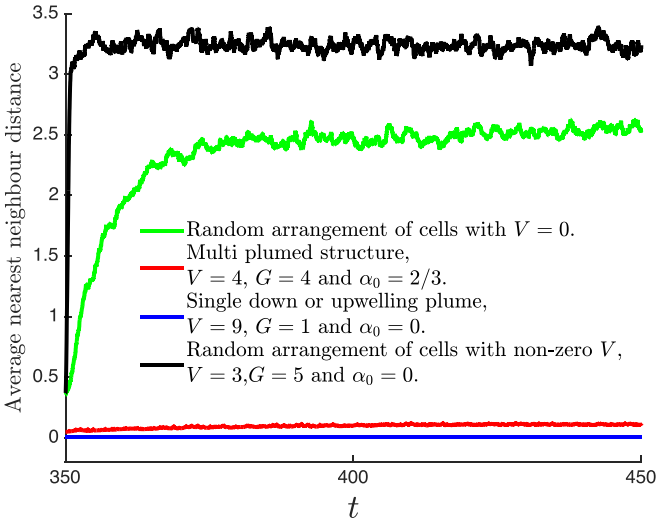

FIG. 14. Distance between cells and their nearest neighbor, averaged over all cells.

To test the robustness of the most intricate structures, the effect of adding small perturbations (noise) to cell orientation was examined. To do this, Eq. (8) was altered to

$$\dot{\boldsymbol{p}} = \begin{pmatrix} -\frac{p_x p_z}{2G} + \frac{\omega_y p_z - \omega_z p_y}{2} + \alpha f_x + \eta\sqrt{1-\xi^2}\cos\theta \\ -\frac{p_y p_z}{2G} + \frac{\omega_z p_x - \omega_x p_z}{2} + \alpha f_y + \eta\sqrt{1-\xi^2}\sin\theta \\ \frac{1-p_z^2}{2G} + \frac{\omega_x p_y - \omega_y p_x}{2} + \alpha f_z + \eta\xi \end{pmatrix}. \tag{26}$$

We take θ and ξ to be uniformly distributed such that $\theta \in [0, 2\pi)$ and $\xi \in [-1, 1]$ adds an additional noise term, uniformly distributed on $\mathbb{S}^2$ with amplitude η. Figure 15 shows four Poincaré sections from the plane $z = 0$, with different values of η when $V = G = 4$ and $\alpha = 2/3$. When $\eta = 0$ there exist nine distinct crossing points which correspond to the nine braids. However, as the level of noise increases so does the number of crossing points. This results in trajectories crossing each other with regularity, meaning the new arrangement is lacking the previous intricate braiding. For parameter ranges which produce single plumes, adding noise revealed that cell aggregation is less focused than before. This causes patterns to be less defined although this does not impede the inherent similarities

TABLE V. ABC flow for values of $V \in [1,9]$, when $G = 4$.

$\alpha = 1$		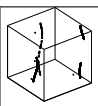	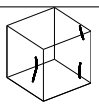	Similar to $V = 3$					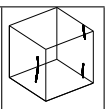
$\alpha = 2/3$	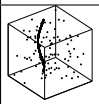	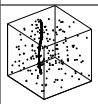	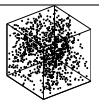	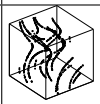	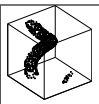	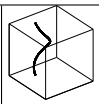	Similar to $V = 6$		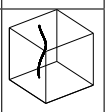
$\alpha = 0$	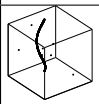	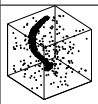	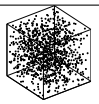	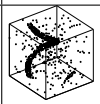	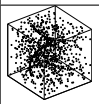	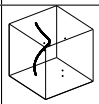	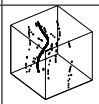	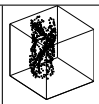	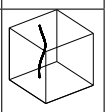
	$V = 1$	$V = 2$	$V = 3$	$V = 4$	$V = 5$	$V = 6$	$V = 7$	$V = 8$	$V = 9$

TABLE VI. ABC flow for values of $G \in [1,9]$, when $V = 4$.

$\alpha = 1$	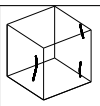	Similar to $G = 1$							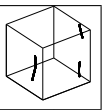
$\alpha = 2/3$	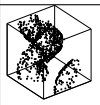	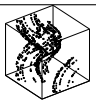	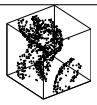	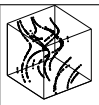	Similar to $G = 4$				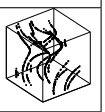
$\alpha = 0$	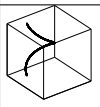	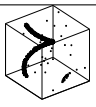	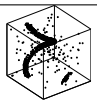	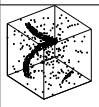	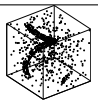	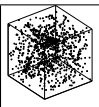	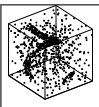	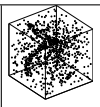	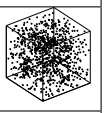
	$G = 1$	$G = 2$	$G = 3$	$G = 4$	$G = 5$	$G = 6$	$G = 7$	$G = 8$	$G = 9$

to structures without noise. The same behavior was seen whether noise was added at $t = 0$ or when the structures had formed.

V. DISCUSSION

Some insight into the role of the shape of the microorganisms and the competition between the vorticity and rate-of-strain terms in the gyrotactic orientation equation [Eq. (5)] can be gained by considering how gyrotaxis varies with α in an axisymmetric flow that approximates a local

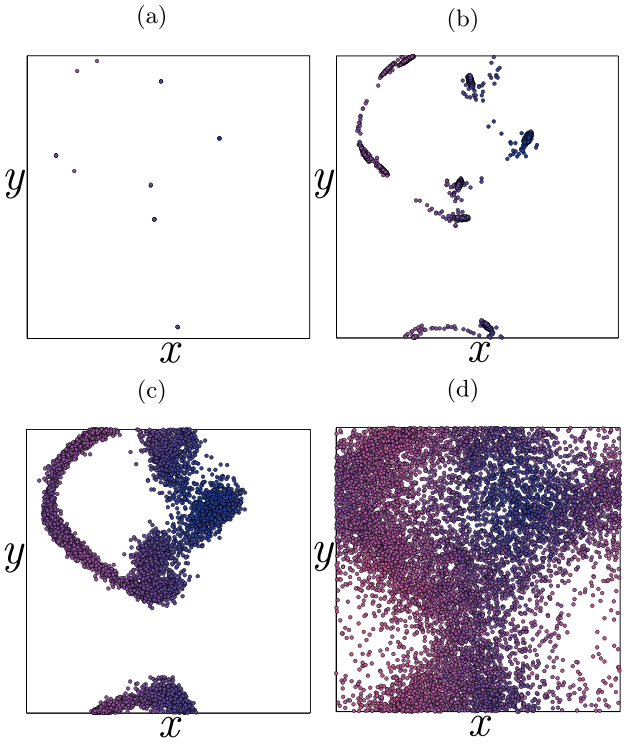

FIG. 15. Poincaré sections in the $z = 0$ plane with $V = G = 4$ and $\alpha = 2/3$, showing the effect of noise on cell trajectories when (a) $\eta = 0$, (b) $\eta = 0.0001$, (c) $\eta = 0.001$, and (d) $\eta = 0.01$.

downwelling region within the imposed periodic flow. Using cylindrical polar coordinates (r,θ,z), suppose the fluid velocity is given by

$$\boldsymbol{u} = w(r)\boldsymbol{k}, \quad \text{where} \quad w(r) = -(L^2 - r^2),$$

which represents downwards Poiseuille flow in a vertical tube of radius L. Writing $\boldsymbol{p}$ in components as $(p_r, p_\theta, p_z)^T$, the gyrotactic balance equation [Eq. (8)] becomes

$$\dot{\boldsymbol{p}} = \frac{1}{2G}\begin{pmatrix} -p_z p_r \\ -p_\theta p_z \\ 1 - p_z^2 \end{pmatrix} - \frac{w'(r)}{2}\begin{pmatrix} p_z - \alpha p_z\left(1 - 2p_r^2\right) \\ 2\alpha p_r p_\theta p_z \\ -p_r - \alpha p_r\left(1 - 2p_z^2\right) \end{pmatrix}, \tag{27}$$

where $w'(r) = 2r$. The only stable steady solution when $0 < \alpha \leqslant 1$ is

$$\begin{aligned} p_r &= \frac{\sqrt{1 - 8\Gamma^2(r)\alpha(1-\alpha)} - 1}{4\Gamma(r)\alpha}, \\ p_\theta &= 0, \quad \text{and} \quad p_z = \sqrt{1 - p_r^2}, \end{aligned} \tag{28}$$

where $\Gamma(r) = Gw'(r)$. In this solution $p_r \leqslant 0$ always and is subject to the additional constraint that

$$p_r \geqslant -1 \Leftrightarrow \begin{cases} \Gamma(1+\alpha) \leqslant 1 & \text{for } 0 < \alpha \leqslant 1/3 \\ \forall \Gamma & \text{for } 1/3 < \alpha \leqslant 1, \end{cases} \tag{29}$$

since $\boldsymbol{p}$ is a unit vector by definition. Moreover, the solution is linearly stable only when $8\Gamma^2\alpha(1-\alpha) < 1$. Combining the two constraints shows that the linearly stable solution exists:

$$\Leftrightarrow \begin{cases} \Gamma(1+\alpha) \leqslant 1 & \text{for } 0 < \alpha \leqslant 1/3 \\ 8\Gamma^2\alpha(1-\alpha) < 1 & \text{for } 1/3 < \alpha \leqslant 1. \end{cases} \tag{30}$$

For the special case $\alpha = 0$,

$$p_r = -\Gamma(r), \quad p_\theta = 0, \quad p_z = \sqrt{1 - \Gamma^2(r)}, \tag{31}$$

which exists and is linearly stable when $0 \leqslant \Gamma < 1$. Thus we see that $p_r \to 0$ as $\alpha \to 1$, i.e., the torques due to local vorticity and rate of strain cancel each other out for rodlike cells, so that the cells swim vertically upwards, even though they are gyrotactic. For details of the other steady but unstable solutions, see [27].

In fact, it is readily shown (although to the best of our knowledge not previously reported) that, for any steady parallel vertical flow of the form $\boldsymbol{u} = w(x,y)\,\boldsymbol{k}$, $\boldsymbol{p} = \boldsymbol{k}$ everywhere is an exact solution of the gyrotactic orientation equation [Eq. (5)] *when* $\alpha = 1$. This shows that rodlike gyrotactic cells focus less well into downwelling flows than more spherical cells, leading to a broadening of cell concentration profiles. In particular when $\alpha = 1$, cells are much less influenced by the ambient flow and tend to swim up at all gyrotaxis numbers, which explains why Lagrangian chaos in the ABC flow is suppressed for all swimming speeds above a critical value as in Figs. 5, 6, and 8. The limit $G \to \infty$, i.e., no gyrotaxis (freely rotating cells), is, of course, singular in that there is no preferred orientation. The results of simulations (see Supplemental Material [26]) for $G = \infty$ in the ABC flow for $\alpha = 0$, 0.5, and 1.0, and $0.1 \leqslant V \leqslant 9.0$ show that in all cases the Lyapunov exponents are positive, so shape alone cannot inhibit mixing in this flow.

We note that the computational results of Bearon *et al.* [28] for 2D particle orientation and trajectories in 2D Poiseuille flow in a channel are consistent with this result, in that the equilibrium cell concentration broadens as α increases.

VI. CONCLUSIONS

Our numerical results, supported by analytical solutions, reveal that gyrotactic cells in incompressible three-dimensional flows can form organized one- or two-dimensional structures for swimming speeds both faster and slower than the ambient flow. These features are not found in the absence of gyrotaxis (see Sec. 4 in the Supplemental Material [26]). The two flows used here are spatially periodic solutions of the Euler equations. In the TGV flow, trajectories collapse ("focus") onto a one-dimensional manifold, except when the cells are spherical, in which case two-dimensional manifolds are also found.

It is of particular interest to note that collapse to a one- or two-dimensional manifold suppresses mixing in the ABC flow, which shape alone cannot do, and complex braids that extend over many spatial periods are seen. Two windows of chaotic trajectories are found as the relative swimming speed V is increased: the first, found when cells do not swim, vanishes as V increases towards 1, while the second occurs over a range of values of $V > 1$. Trapping in islands, which is a feature of 2D flows [7–9], is not seen in the 3D ABC flow. Furthermore, these results are robust, in that the structures persist in the presence of noise, suggesting that both the inhibition of Lagrangian chaos by gyrotactic focusing and the reemergence of chaos may be biologically relevant in taking advantage of the local flow environment for aggregation or mixing, outside of carefully controlled laboratory environments.

A further observation is that (as noted in the discussion of Fig. 7) robust structures form in the ABC flow for values of $V \approx 0.01$ which is some five times smaller than required in the TGV flow. Whether this is specific to these two flows or is a more general result that the presence of Lagrangian chaos enhances the formation of structures merits further study beyond the scope of this paper.

ACKNOWLEDGMENT

This research was funded by an EPSRC Ph.D. scholarship awarded to S.I.H.R.

[1] G. Subramanian and P. R. Nott, The fluid dynamics of swimming microorganisms and cells, J. Indian Inst. Sci. **91**, 383 (2011).

[2] J. S. Guasto, R. Rusconi, and R. Stocker, Fluid mechanics of planktonic microorganisms, Annu. Rev. Fluid Mech. **44**, 373 (2012).

[3] A. D. Barton, S. Dutkiewicz, G. Flierl, J. Bragg, and M. J. Follows, Patterns of diversity in marine phytoplankton, Science **327**, 1509 (2010).

[4] W. M. Durham and R. Stocker, Thin phytoplankton layers: Characteristics, mechanisms, and consequences, Annu. Rev. Mar. Sci. **4**, 177 (2012).

[5] G. J. Thorn and R. N. Bearon, Transport of spherical gyrotactic organisms in general three-dimensional flow fields, Phys. Fluids **22**, 041902 (2010).

[6] M. A. Bees and O. A. Croze, Mathematics for streamlined biofuel production from unicellular algae, Biofuels **5**, 53 (2014).

[7] C. Torney and Z. Neufeld, Transport and Aggregation of Self-Propelled Particles in Fluid Flows, Phys. Rev. Lett. **99**, 078101 (2007).

[8] N. Khurana, J. Blawzdziewicz, and N. T. Ouellette, Reduced Transport of Swimming Particles in Chaotic Flow due to Hydrodynamic Trapping, Phys. Rev. Lett. **106**, 198104 (2011).

[9] N. Khurana and N. T. Ouellette, Interactions between active particles and dynamical structures in chaotic flow, Phys. Fluids **24**, 091902 (2012).

[10] W. M. Durham, E. Climent, and R. Stocker, Gyrotaxis in a Steady Vortical Flow, Phys. Rev. Lett. **106**, 238102 (2011).

[11] T. J. Pedley and J. O. Kessler, The orientation of spheroidal microorganisms swimming in a flow field, Proc. R. Soc. B **231**, 47 (1987).
[12] W. M. Durham, E. Climent, M. Barry, F. De Lillo, G. Boffetta, M. Cencini, and R. Stocker, Turbulence drives microscale patches of motile phytoplankton, Nat. Commun. **4**, 2148 (2013).
[13] O. A. Croze, G. Sardina, M. Ahmed, M. A. Bees, and L. Brandt, Dispersion of swimming algae in laminar and turbulent channel flows: Consequences for photobioreactors, J. R. Soc. Interface **10**, 20121041 (2013).
[14] A. Wolf, J. B. Swift, H. L. Swinney, and J. A. Vastano, Determining Lyapunov exponents from a time series, Physica D **16**, 285 (1985).
[15] G. Haller and G. Yuan, Lagrangian coherent structures and mixing in two-dimensional turbulence, Physica D **147**, 352 (2000).
[16] G. I. Taylor, On the decay of vortices in a viscous fluid, Philos. Mag. **46**, 671 (1923).
[17] G. I. Taylor and A. E. Green, Mechanism of the production of small eddies from large ones, Proc. R. Soc. London A **158**, 499 (1937).
[18] T. Dombre, U. Frisch, J. M. Greene, M. Hénon, A. Mehr, and A. M. Soward, Chaotic streamlines in the ABC flows, J. Fluid Mech. **167**, 353 (1986).
[19] X.-H. Zhao, K.-H. Kwek, J.-B. Li, and K.-L. Huang, Chaotic and resonant streamlines in the ABC flow, SIAM J. Appl. Math. **53**, 71 (1993).
[20] T. J. Pedley and J. O. Kessler, Hydrodynamic phenomena in suspensions of swimming microorganisms, Annu. Rev. Fluid Mech. **24**, 313 (1992).
[21] T. Ishikawa, J. T. Locsei, and T. J. Pedley, Development of coherent structures in concentrated suspensions of swimming model micro-organisms, J. Fluid Mech. **615**, 401 (2008).
[22] N. Bowditch, On the motion of a pendulum suspended from two points, Mem. Am. Acad. Arts Sci. **3**, 413 (1815).
[23] J. Ottino, Mixing, chaotic advection, and turbulence, Annu. Rev. Fluid Mech. **22**, 207 (1990).
[24] D. Saintillan and M. J. Shelley, Instabilities and Pattern Formation in Active Particle Suspensions: Kinetic Theory and Continuum Simulations, Phys. Rev. Lett. **100**, 178103 (2008).
[25] L. H. Cisneros, R. Cortez, C. Dombrowski, R. E. Goldstein, and J. O. Kessler, Fluid dynamics of self-propelled microorganisms, from individuals to concentrated populations, Exp. Fluids **43**, 737 (2007).
[26] See Supplemental Material at http://link.aps.org/supplemental/10.1103/PhysRevFluids.3.023102 for the full range of parameter values that have been used in simulations of the ABC and TGV flows.
[27] S. Heath Richardson, Pattern formation by swimming micro-organisms in chaotic flows, turbulence and bioconvection, Ph.D. thesis, University of Glasgow, 2018.
[28] R. N. Bearon, A. L. Hazel, and G. J. Thorn, The spatial distribution of gyrotactic swimming micro-organisms in laminar flow fields, J. Fluid Mech. **680**, 602 (2011).